Ultrasound in Med. & Biol., Vol. xx, No. x, pp. xxx, 2009

0301-5629/09/$–see front matter

ELSEVIER

doi:10.1016/j.ultrasmedbio.2008.10.001

● *Original Contribution*

MICROVASCULAR FLOW ESTIMATION BY MICROBUBBLE-ASSISTED NAKAGAMI IMAGING

PO-HSIANG TSUI,* CHIH-KUANG YEH,† and CHIEN-CHENG CHANG,*‡

*Division of Mechanics, Research Center for Applied Sciences, Academia Sinica, Taipei Taiwan; †Department of Biomedical Engineering and Environmental Sciences, National Tsing Hua University, Hsinchu, Taiwan; and ‡Institute of Applied Mechanics, National Taiwan University, Taipei, Taiwan

(*Received* 25 *January* 2008; *revised* 19 *September* 2008; *in final form* 2 *October* 2008)

Abstract— The destruction and replenishment of microbubbles has been previously applied to estimating blood flow in the microcirculation. The rate of increase of the time–intensity curve (TIC) due to microbubbles flowing into the region-of-interest (ROI) as measured from the conventional B-mode images reflects the flow velocity. In this study, we monitored microbubble replenishment using a new proposed approach called the time–Nakagami-parameter curve (TNC) obtained from the parametric image based on the Nakagami statistical parameter for quantifying the microvascular flow velocity. The Nakagami parameter is estimated from signal envelope to reflect the backscattered statistics. The feasibility of using the TNC to estimate the microvascular flow was explored by carrying out phantom measurements and *in vivo* animal experiments. The rates of increase of the TIC and TNC were quantified as the rate constants β_I and β_N of monoexponential fitted curves, respectively. The experimental results showed that β_N behaves similarly to the conventional β_I in quantifying the flow velocity. Moreover, the tolerance to the effects of clutter is greater for the TNC than for the TIC, which makes it possible to use β_N to differentiate various flow velocities even when the ROI contains nonperfused areas. This finding suggests that the TNC-based technique can be used as a complementary tool for the conventional TIC to improve measurement of blood flow in the microcirculation. (E-mail: ckyeh@mx.nthu.edu.tw)

Key Words: **Microcirculation, Nakagami parameter, Microbubble, Contrast agent.**

INTRODUCTION

Microvascular changes occur in many disease states, including cancer and diabetes (Weidner et al. 1991), with current treatments focusing on controlling angiogenesis to modulate blood perfusion in tissues. There is considerable evidence that the prognosis is linked to the specific microvascular morphology (Folberg et al. 1992; Makitie et al. 1999) and, hence, estimating the blood flow in the microcirculation in tissues is of great importance to clinical diagnosis and prognosis.

Several noninvasive imaging modalities can be applied to measure the blood flow in the microcirculation, such as single-photon-emission computed tomography, positron-emission tomography and magnetic resonance imaging. However, the associated high costs and long examination periods limit the availability and popularization of these techniques (Schlosser et al. 2001). In contrast, ultrasound imaging is a widely available and relatively inexpensive method for estimating the blood flow. However, there remain some limitations when using conventional ultrasound imaging to evaluate microvascular changes. First, the vessel sizes within the microcirculation range from 5 to 200 μm (with flow velocities from 0.1 to 10 mm/s) (Fung 1997), which means that the spatial resolution of conventional Doppler ultrasound systems operating at 2–10 MHz is insufficient. Second, the typical weakness of ultrasonic signals backscattered from blood in microvascular structures makes it difficult for flow information to be obtained using a conventional ultrasound system.

To overcome the above problems of conventional ultrasound, microvascular flows are generally estimated using high-frequency ultrasound imaging combined with a microbubble contrast agent. Using high-frequency ultrasound can simultaneously enhance the image resolution and the backscattering coefficient of blood and injecting microbubbles into the blood can enhance the

Address correspondence to: Chih-Kuang Yeh, Department of Biomedical Engineering and Environmental Sciences, National Tsing Hua University, 101, Section 2, Kuang-Fu Road, Hsinchu 30013, Taiwan. E-mail: ckyeh@mx.nthu.edu.tw

backscattering intensity and contrast of flow signals so as to improve the sensitivity. A popular contrast-enhanced imaging method is the microbubble destruction and replenishment technique (Wei et al. 1998). In this method, after microbubbles are destroyed by a low-frequency, high mechanical index ultrasound pulse, the intact microbubbles flowing into the sample volume can be monitored over time by B-scans to obtain the so-called time–intensity curve (TIC). Wei et al. (1998) proposed a monoexponential function to model the TIC and quantified the rate of increase of the TIC using the rate constant β, which is proportional to the blood flow velocity. Based on the exponential model of the TIC, Yeh et al. (2004) further developed a 25-MHz high-frequency microbubble destruction and replenishment imaging system with a spatial resolution of $160 \times 160\ \mu m^2$ to estimate the microvascular flow velocity. Although the TIC determined for cerebral and renal tissue perfusion is not well represented by an exponential function, instead requiring a sigmoid-based model for good agreement (Krix et al. 2003; Lucidarme et al. 2003; Metoki et al. 2006), the rate constant obtained by fitting the TIC using the monoexponential model is still a useful and popular index for estimating the blood flow.

One difficulty that arises when measuring the TIC is that the ultrasonic echoes acquired from the region-of-interest (ROI) often include both signals backscattered from the microbubbles and clutter echoes contributed by the nonperfused areas mainly containing the surrounding tissues and vessel walls. The clutter signals typically appear at low frequencies and at 40–60 dB higher than the blood signal (Bjærum and Torp 2002; Feng et al. 2006). Although injecting microbubbles into the blood can enhance the intensity of the flow signal, this enhancement is typically only 8–25 dB (Forsberg et al. 1998), which means that the clutter components may still greatly affect the flow signals and the TIC. For this reason, a high-pass filter (*i.e.,* wall filter) is often applied to separate the clutter echoes from the flow signals (Tao et al. 2004; Feng et al. 2006). A fixed wall filter usually does not provide optimal filtering but using an adaptive filter may increase the computational complexity. In addition, the bandwidth of the signals associated with low flow velocities may overlap with that of the clutter signals, resulting in filtering also removing some of the flow information (Tao et al. 2004). More importantly, applying a wall filter to remove the clutter components does not necessarily produce an effective TIC for estimating the flow velocity (Yeh et al. 2004).

To produce an acceptable TIC for estimating the flow velocity, we start to study the feasibility of using ultrasound parametric images that are independent of the backscattering intensity (*i.e.,* not conventional B-mode images) to monitor the microbubble replenishment. Our rationale comes from the aim of reducing the dependence of the TIC on signal amplitude. A new parametric imaging method based on the Nakagami statistical parameter recently proposed by the present authors (Tsui and Chang 2007) is particularly suitable for measuring the microbubble replenishment. This is because the Nakagami-parameter map (Nakagami image) is independent of the backscattering intensity, allowing visualization of only the scatterer concentrations in the scattering medium by analyzing the probability density function (pdf) of the backscattered signals. This study explored the feasibility of using the time–Nakagami-parameter curve (TNC) for microvascular flow measurements.

In the remainder of this article, we first introduce the theoretical background for the Nakagami statistical distribution and the microbubble destruction and replenishment imaging model and then describe the materials and methods used for phantom measurements and *in vivo* animal experiments. The 25-MHz B-mode and Nakagami images acquired from flow phantoms and the rabbit eye for different flow velocities were used to calculate the TIC and TNC. We applied the monoexponential model to fit the TIC and TNC to explore the feasibility of using parameter β to quantify the flow velocity in the microcirculation. Finally, we discuss and remark on the advantages and potential of using the TNC over the conventional TIC for estimating blood flow in the microcirculation.

THEORETICAL BACKGROUND

Nakagami distribution

The Nakagami model was initially proposed to describe the statistical distribution of radar echoes (Holfman 1960). Since the late 1980s, it has been widely applied to the statistical analysis of ultrasonic backscattered signals (Hampshire et al. 1988; Zimmer et al. 1996; Shankar 2000; Wachowiak et al. 2002). The Nakagami distribution is a general model that describes all the scattering conditions in medical ultrasound, including pre-Rayleigh, Rayleigh and post-Rayleigh distributions (Shankar 2000). The pdf $f(r)$ of the ultrasonic backscattered envelope R under the Nakagami statistical model is given by

$$f(r) = \frac{2m^m r^{2m-1}}{\Upsilon(m)\Omega^m}\exp\left(-\frac{\mathrm{m}}{\Omega}r^2\right)U(r), \qquad (1)$$

where $\Gamma(.)$ and $U(.)$ are the gamma function and the unit step function, respectively. Let $E(.)$ denote the statistical mean, then the scaling parameter Ω and the Nakagami parameter m associated with the Nakagami distribution can be respectively obtained from

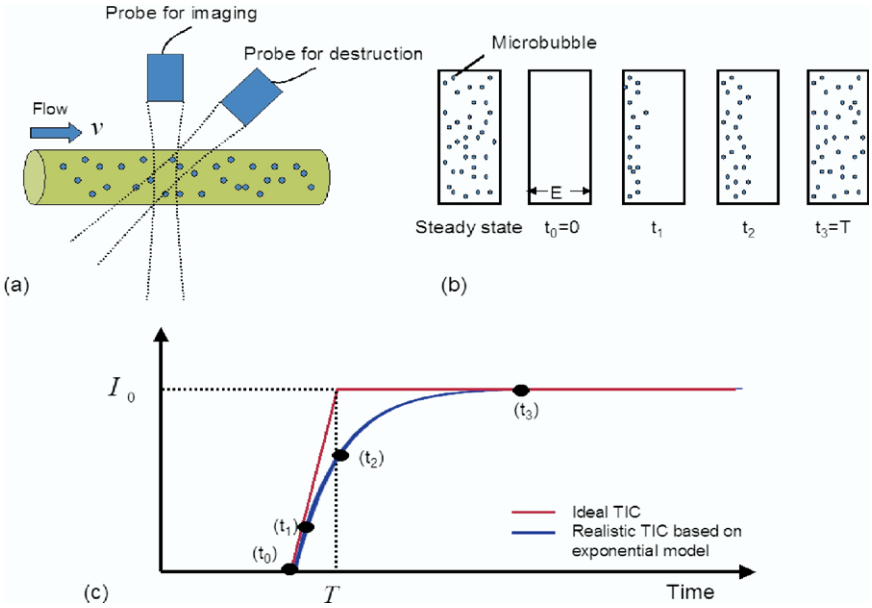

Fig. 1. Microbubble destruction and replenishment imaging model based on a monoexponential function.

$$\Omega = E(R^2) \tag{2}$$

and

$$m = \frac{[E(R^2)]^2}{E[R^2 - E(R^2)]^2} \tag{3}$$

Nakagami parameter m is a shape parameter that is determined by the pdf of the ultrasonic backscattered envelope. As m varies from 0 to 1, the statistics of the envelope change from a pre-Rayleigh to a Rayleigh distribution and the backscattered statistics conform to a post-Rayleigh distribution if m is larger than 1. It should be noted that the envelope statistics conform to a Rayleigh distribution when the resolution cell of the ultrasonic transducer contains a large number of randomly distributed scatterers (Burckhardt 1978). Moreover, if the resolution cell contains scatterers that have randomly varying scattering cross-sections with a high degree of variance, the envelope statistics conform to a pre-Rayleigh distribution. Finally, if the resolution cell contains periodically located scatterers in addition to randomly distributed scatterers (or there are locally a large number of scatterers present), the envelope statistics conform to a post-Rayleigh distribution (Shankar 2000; Shankar et al. 2001). Therefore, Nakagami model is an outstanding methodology for characterizing the scattering medium.

Microbubble destruction and replenishment imaging model

Figure 1 that is adapted from Wei et al. 1988 illustrates the microbubble destruction/replenishment imaging model. The infusion with a contrast agent at a constant rate and concentration will produce a steady-state concentration throughout the circulation after a certain period of time. When the subsequent local application of high-pressure pulses destroys microbubbles within a sample volume with a width of E, the echo intensity would suddenly drop and intact microbubbles will then enter this volume at a rate determined by the flow velocity v and vessel topology. At a constant v, the microbubbles finally fill the entire beam volume and the echo intensity I will gradually recover to the original backscattering intensity I_0 at time T according to

$$E = vT \tag{4}$$

Such a change in the backscattered echo intensity as a function of time is the so-called TIC. The ideal TIC is indicated by the dotted line in Fig. 1c. However, the profile of the microbubble concentration is not expected to be entirely flat. Therefore, Wei et al. (1998) proposed a monoexponential function to model the TIC. In a more general form, we can write down the monoexponential model of the TIC as follows

$$I = I_c + (I_0 - I_c) \cdot (1 - ce^{-\beta(t-t_0)}) \tag{5}$$

where I_C is the clutter echo intensity introduced to consider the background intensity, β is the constant related to the rate at which the echo intensity increases and the parameter c is used to describe the degree of partial destruction of microbubbles. Note that I_0 and β would be also affected by the partial microbubbles destruction

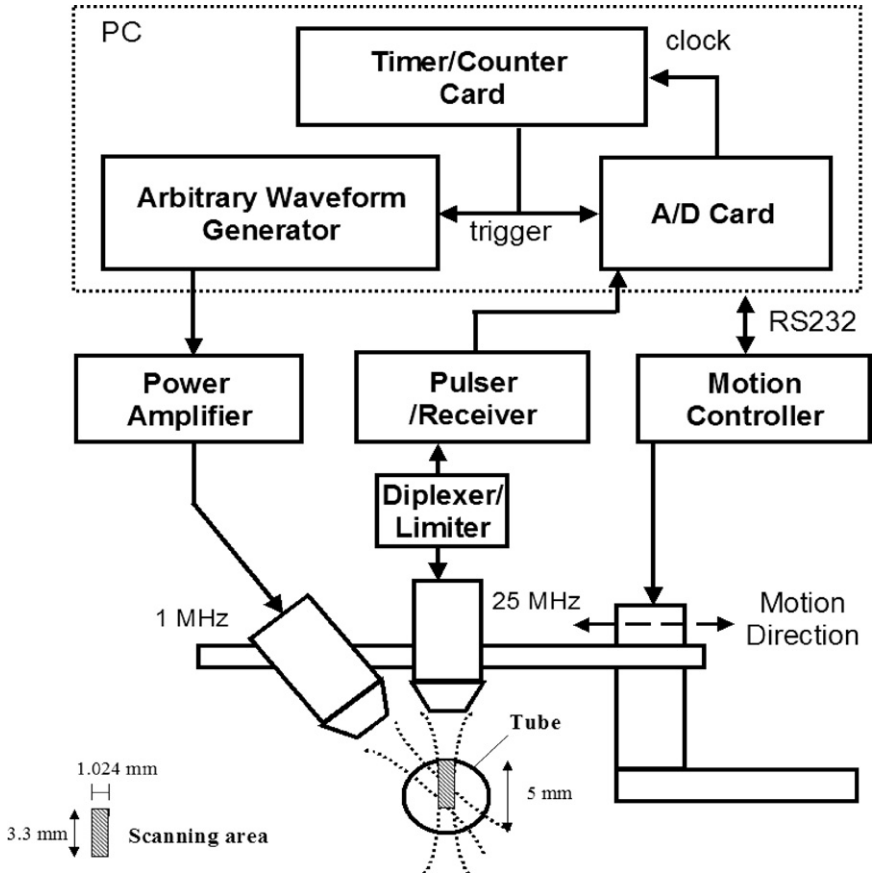

Fig. 2. Block diagram of the microbubble destruction and replenishment experimental set-up.

(Leong-Poi et al. 2005). In case the clutter signals have been thoroughly removed ($I_C = 0$), the microbubbles have been fully destroyed ($c = 1$) and the intensity begins to rise at $t_0 = 0$, eqn 5 can be simplified as

$$I = I_0 \cdot (1 - e^{-\beta t}) \tag{6}$$

Equation 6 is illustrated by the solid line in Fig. 1c. Taking the first-order derivative of eqn 6 yields

$$I' = I_0 \beta e^{-\beta t} \tag{7}$$

Thus, the tangent slope of the TIC based on the exponential model at the origin ($t = 0$) is

$$s = I_0 \beta. \tag{8}$$

Figure 1c shows that s is also equal to I_0/T and, hence,

$$\beta = \frac{1}{T} \tag{9}$$

Consequently, the flow velocity can be calculated as

$$v = E\beta \tag{10}$$

and the flow rate f can be further estimated by the product of A (the cross-sectional area) with v (the flow velocity):

$$f = Av \tag{11}$$

Equations 9 and 10 indicate that the blood flow velocity can be quantified using β if the characteristics of the ultrasound beam are known. The time to achieve 99% replenishment, $T_{99\%}$, is used to estimate β based on the monoexponential model in eqn 6:

$$\beta = \frac{-\ln(0.01)}{T_{99\%}} \tag{12}$$

METHODS

System description

Figure 2 shows a block diagram of the microbubble destruction and replenishment imaging system. The major components included those for pulse generation, data acquisition and motor control. The system consisted of two single-element transducers with spherical focusing:

Table 1. Specifications of transducers

	Destruction (V303)	Imaging (V324)
Center frequency	1 MHz	25 MHz
Element diameter (mm)	12.70	6.35
Focal length (mm)	15.01	12.85
−6 dB bandwidth	78.2%	51.5%
−6 dB (−3 dB) depth of focus (mm)	15.54 (8.29)	1.40
−6 dB (−3 dB) lateral beam width (mm)	11.09 (7.99)	0.12
−6 dB (−3 dB) elevational beam width (mm)	3.24 (2.36)	0.12

(1) a 25-MHz spherically focused transducer (Model V324, Panametrics-NDT, Waltham, MA, USA) used for high-resolution imaging and (2) a 1-MHz cylindrically focused transducer (Model V303, Panametrics-NDT) used for microbubble destruction. These two transducers were fixed in a machined holder in a confocal arrangement. The 25-MHz imaging elevational plane was aligned perpendicular to the flow direction. The sound profiles and focal lengths of two transducers were measured using a wideband hydrophone (Model HNP-0400, ONDA, Sunnyvale, CA, USA) mounted on a positioner controlled by a three-dimensional stepping motor. The central frequencies and bandwidths of the transducers were then estimated using Fourier spectra of the echoes acquired from the focal zone. The specifications of the two transducers are summarized in Table 1.

The pulser/receiver (Model 5900PR, Panametrics-NDT) provided impulse excitation to the 25-MHz transducer for transmitting acoustic pulses and receiving the radio-frequency (RF) ultrasound backscattered signals through a transformer diplexer/diode limiter circuit for protection purposes. The excitation energy was 8 μJ, which produced an acoustic pressure of 0.24 MPa at the transducer focal zone (as measured by a hydrophone). The received RF backscattered signals were amplified by a low-noise preamplifier (Model AU-1114-BNC, Miteq, Hauppauge, NY, USA) and then further amplified 42 dB by the built-in amplifier in the pulser/receiver. Finally, the backscattered signals were digitized at a 120-MHz sampling rate using a 14-bit analog-to-digital card (Model PCI-9820, Adlink, Taipei, Taiwan) and stored on a PC for off-line processing. The 1-MHz pulses with a length of 10 cycles used to destroy microbubbles were generated by a programmable arbitrary-waveform generator (Model 5300, Tabor Electronics, Tel Hanan, Israel) and then amplified by an RF power amplifier (Model 150A100B, AR, Bothell, WA, USA) to produce an acoustic pressure of 0.7 MPa at the transducer focal region. We previously showed that more than 95% of the microbubbles can be destroyed by 10 cycles of a 1-MHz pulse at 0.6 MPa (Yeh et al. 2005).

Phantom measurements

The flow phantom was constructed by embedding a dialysis tube with an inner diameter of 5 mm and a thickness of 0.5 mm into an agar phantom formed by dissolving 2 g of agar powder in 100 mL of water. The commercial ultrasound contrast-agent Definity® (Bristol-Myers Squibb, New York, NY, USA) was used at a concentration 40 μL (μl) of contrast agent per 100 mL of water. A syringe pump was used to control the flow rate from 30 to 400 mL/h, corresponding to a mean flow velocity from 0.42 to 5.66 mm/s. A magnetic stirring bar inside the syringe was used to keep the solution well mixed. A flexible rubber buffer made of latex with the characteristics of lower attenuation between the phantom and the syringe pump was used to dampen pulsatile flow and vibration produced by the syringe pump.

When the microbubble solution was stably flowing in the tube, we scanned the flow phantom with the 25-MHz transducer at 10 frames/s to monitor the movement of the microbubbles in the solution. The scanning area consisted of 64 A-lines, where the distance between each A-line was 16 μm, which corresponds to approximately 3.3 $\times$ 1.024 mm^2. After 2 s of data acquisition, the 1-MHz transducer was switched on to destroy the microbubbles. The total acquisition time was 12 s, corresponding to 120 images. For each image, all the scan lines of the ultrasonic backscattered signals were demodulated by taking their absolute values of Hilbert transform to obtain the envelope image. The B-mode images were displayed as typically log-compressed envelope images with a dynamic range of 40 dB. We then processed the data according to our previous studies (Tsui and Chang 2007), where the Nakagami image was constructed from the Nakagami-parameter map obtained by using the sliding window technique to process the uncompressed envelope image. The size of the sliding window was 480 $\times$ 480 μm^2 – the use of a square with a side length equal to three times the pulse length of the incident ultrasound (*i.e.,* approximately 160 μm) satisfies a stable estimation of the local Nakagami parameter based on eqn 3 (Tsui and Chang 2007). Pseudocolor was used to clearly display the values of the Nakagami parameter in the Nakagami image: values from 0 to 1 were shaded from dark blue to light blue, representing backscattered envelopes exhibiting statistics of varying pre-Rayleigh distributions; values of 1 were shaded white, representing a Rayleigh distribution; and those larger than 1 were shaded from light red to dark red, representing backscattered envelopes exhibiting statistics of varying post-Rayleigh distributions.

To estimate the flow velocities at different depths in

the phantom, we measured the TICs and TNCs in three ROIs of size 480 × 480 μm^2 in the scanning region: ROIs 1, 2 and 3 were located at depths of 1.28, 1.92 and 2.56 mm, respectively. The TIC was obtained from the temporal changes in the backscattering intensity calculated by averaging all pixels in the ROI of the echo intensity image obtained from the square of the envelope image and the TNC based on the Nakagami image was obtained analogously. Consequently, the average values of β based on the TIC (β_I) and TNC (β_N) as functions of the flow velocity were obtained using eqn 12 from five phantom measurements. In addition, to simulate the tissue clutter components and explore their influences on flow estimation by the TIC and TNC, we placed a small amount of cotton (less than 0.01 g) inside the flow phantom and repeated the above experimental procedure. Note that the cotton needs to be placed into the water first and to be centrifuged then to eliminate the air in the cotton. After this process, we stuffed the cotton into the tube in the water bath. Such cotton simulates not only the tissue scattering but also the flow randomization in the microcirculation.

In vivo animal experiments

The performance of using the TNC technique to estimate the microvascular flow was further explored by performing an *in vivo* animal experiment in which the highly vascular ciliary body and iris region of a healthy Dutch Belt rabbit eye was imaged. The rabbit eye is an acceptable physiologically relevant model for microvascular blood flow (Silverman et al. 1999; Yeh et al. 2004). The rabbit was first anesthetized with an IM injection of diazepam at 5 mg/kg followed by 2.5% isoflurane. A small speculum was used to fix the eyelids and ultrasound gel is applied to the eye. An acoustic window at the bottom of a water bath was placed in contact with the gel and filled with distilled water. The water was maintained at 40°C using a temperature controller and the contrast agent was injected through an ear vein at full concentration (directly from the vial) using a syringe pump set to 0.5 mL/h. When the microbubbles were flowing stably in the eye blood vessels, the 25-MHz transducer began to scan the 2.5 × 2.0 mm^2 region containing the iris and ciliary process at 10 frames/s. We then switched on the 1-MHz transducer to destroy the microbubbles and simultaneously data were acquired for 10 s to collect a total of 100 images for monitoring the replenishment of microbubbles. Each image consisted of 128 A-lines of backscattered signals with 512 sample points obtained at a sampling rate of 125 MHz. Speckle tracking was applied to align subsequent images so as to reduce physiological motion artifacts. Furthermore, a step-initialized, second-order inverse-Chebyshev high-pass filter with a –30 dB stopband and –1.5 dB passband frequencies of 1.7 and 2.1 Hz was used in the image index dimension for wall filtering. The filter was first applied in the forward direction and then reapplied in the reverse direction to cancel nonlinear phase distortion. Note that both the envelope intensity and Nakagami parameter values corresponding to each image were formed before and after applying wall filtering and a sliding window of size 480 × 480 μm^2 was used to measure the local TIC and TNC for constructing the β_I and β_N parametric images of the scanning region. Five independent measurements were repeated to confirm the reproducibility of the results.

RESULTS AND DISCUSSION

Flow phantom without cotton

The precontrast (no microbubble), microbubble destruction and replenishment B-mode and Nakagami images of the flow phantom without cotton are shown in Fig. 3. The precontrast image is shown in Fig. 3a. Typical B-mode images obtained at 0.7, 2.2, 2.5, 3.0 and 3.6 s are shown in Fig. 3b through f, respectively. Here the flow velocity was 1.27 mm/s, corresponding to a flow rate of 90 mL/h. Figure 3b is the predestruction image. Excitation with the 1-MHz pulse to destroy the microbubbles darkened the B-mode image in the flowing region, as shown in Fig. 3c and the progressive replenishment of the microbubbles resulted in the echoic area (bright portions) of the B-mode image gradually expanding, as indicated by Fig. 3d and f.

The Nakagami images corresponding to the B-mode images in Fig. 3a through f are shown in Fig. 3g through l. The predestruction Nakagami image (Fig. 3h) exhibits more blue shading in the upper portion of the flow phantom at depths from 0 to 1.5 mm and more red shading for depths larger than 1.5 mm. The reason why the Nakagami image has more blue shading in the upper portion of the flow phantom and more red shading for deeper locations may be due to attenuation. This is because the noise would become larger when the attenuation is stronger, making the global envelope statistics close to Rayleigh distribution (Tsui et al. 2005). In this condition, there would be more local red regions of post-Rayleigh statistics appearing in the Nakagami image (Tsui et al. 2008). Figure 3i shows the Nakagami image at the moment of microbubble destruction. There are no red areas evident, with dark blue being the predominant shading in the Nakagami image, which is due to most of the microbubbles being destroyed. The subsequent progressive replenishment of the microbubbles results in a gradual increase in the microbubble concentration in the sample volume and, hence, the Nakagami image recovers its original blue/red-interlaced shading, as shown in Fig. 3j through l.

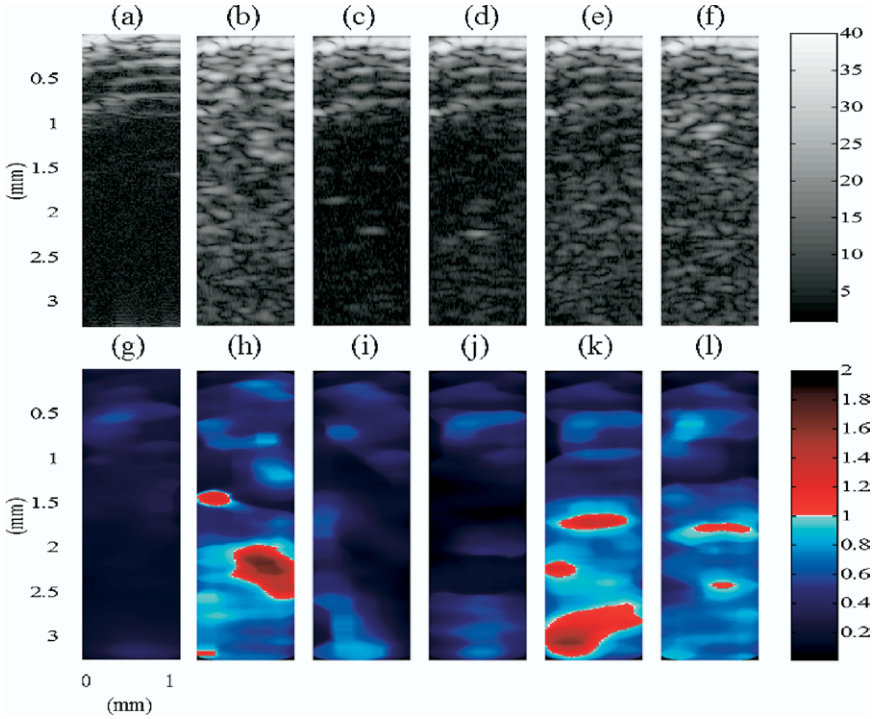

Fig. 3. Typical precontrast (a), postcontrast (b), destruction (c) and replenishment B-mode (d) and (f) and their corresponding Nakagami (g) through (l) images for a flow velocity of 1.27 mm/s (no cotton inside the flow phantom).

Typical TICs for a flow velocity of 1.27 mm/s in different ROIs obtained from the B-mode images are shown in Fig. 4a through c, which indicates that the normalized backscattering intensity increases with the replenishment time, eventually approaching a steady-state value when the microbubbles are fully replenished in the scan volume. It is obvious from the figure that the TICs of different ROIs can be fitted well with an increasing monoexponential function, which is in good agreement with previous experimental studies (Wei et al. 1998, 2001; Chomas et al. 2001; Yeh et al. 2004). The TNCs of different ROIs for the same velocity of 1.27 mm/s obtained from the Nakagami images are shown in Fig. 4d through f. The TNCs gradually increase with the replenishment time, due to increasing numbers of microbubbles in the sample volume increasing the average Nakagami parameter, eventually reaching a steady state when the intact microbubbles are fully replenished in the entire scan volume. Note that the TNCs and their monoexponential fittings reveal two important points. First, based on the plateau phase of the TNC, the microbubble concentration may differ with depth in the flow phantom. Although this information was also indicated by the previous results of the Nakagami image, using the TNC can be more quantitative. With an increase in the image depth, the average Nakagami parameter of the TNC plateau phase tends to vary from 0.65 to 0.85, corresponding to a change in the backscattered statistics from a pre-Rayleigh to an approximate Rayleigh distribution, indicating that there are more microbubbles in the center of the flow phantom. Second, the exponential model also fits the TNC well, showing that the behavior of the TNC is very similar to that of the TIC, although the slopes during the increasing phases of the TIC and TNC are not identical. Therefore, it is appropriate to apply the monoexponential function to model the TNC for estimating the flow velocity in high-frequency measurements. It is especially interesting that the slope during the increasing phase is steeper (*i.e.*, faster rise time) for the TNC based on the Nakagami image than for the B-scan-based TIC. This is due to the characteristics of the statistical parameter. Previous study has shown that the ultrasound statistical parameter would earlier tell the initial point of the plateau phase compared with the intensity-based parameter (Huang et al. 2007). This suggests that the Nakagami image has a faster response time and is more sensitive for detecting the microbubble replenishment following their destruction.

Further comparison between Fig. 4a through c and Fig. 4d through f reveals another point: that the TNC may be more suitable than the TIC for quantifying the microbubble concentration because the former depends only on the change in the backscattered statistics caused by the variation in microbubble concentration and is

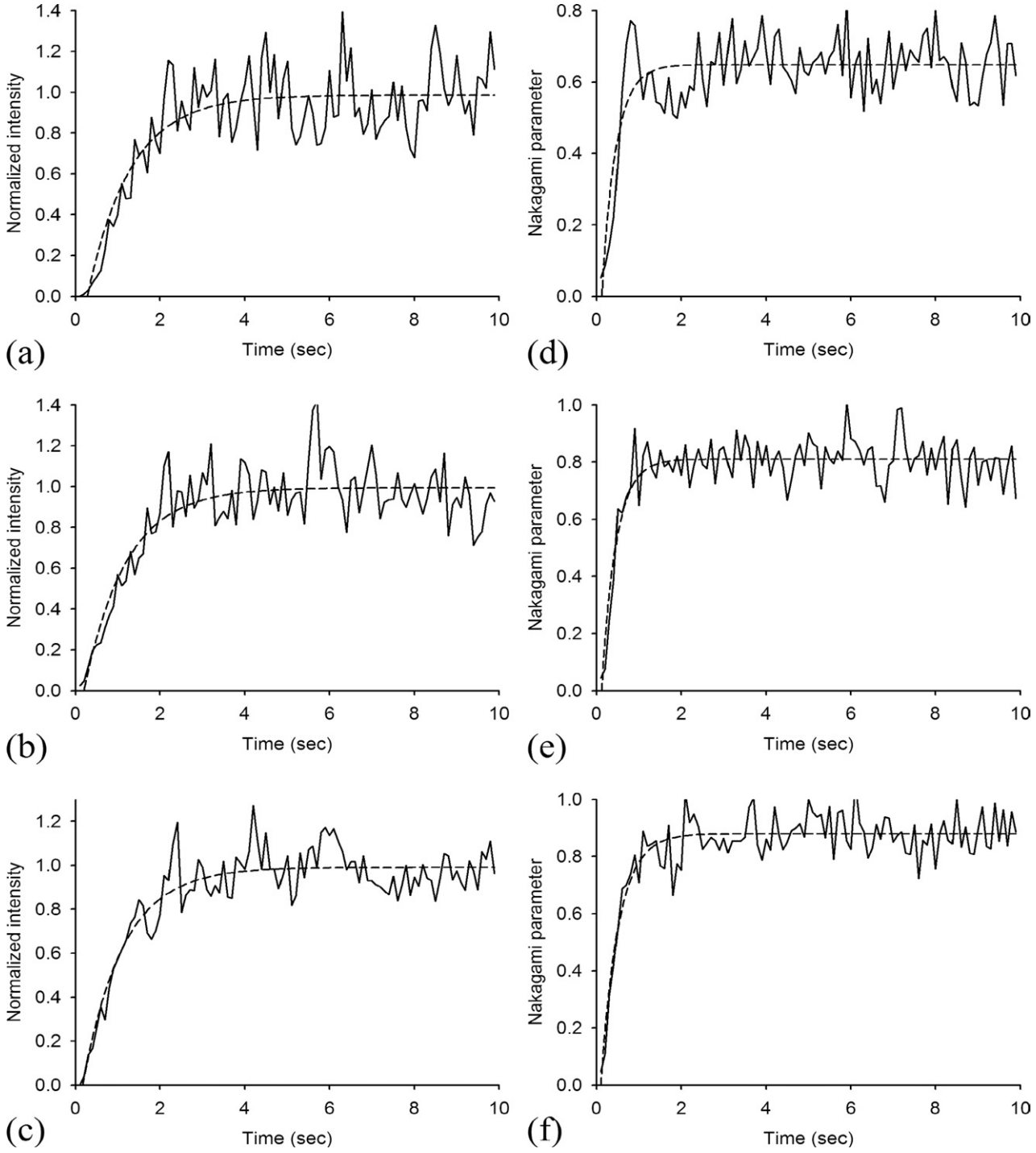

Fig. 4. Time–intensity curves (TICs) (a) through (c) and time–Nakagami-parameter curve (TNCs) (d) through (f) for a flow velocity of 1.27 mm/s in regions-of-interest (ROIs) at depths of 1.28, 1.92 and 2.56 mm, respectively (no cotton inside the flow phantom).

independent of the echo amplitude that is easily affected by the pulse energy and the system gain.

Now we show the values obtained for constants β_I and β_N based on the TIC and TNC, respectively, as functions of flow velocity (Fig. 5). For three ROIs at different depths, the average β_I increased from approximately 2/s to 10/s as the flow velocity increased from 0.42 to 5.66 mm/s (Fig. 5a through c) and the average β_N based on the TNC also increased from approximately 2/s to 10/s for the same increase in flow velocity (Fig. 5d

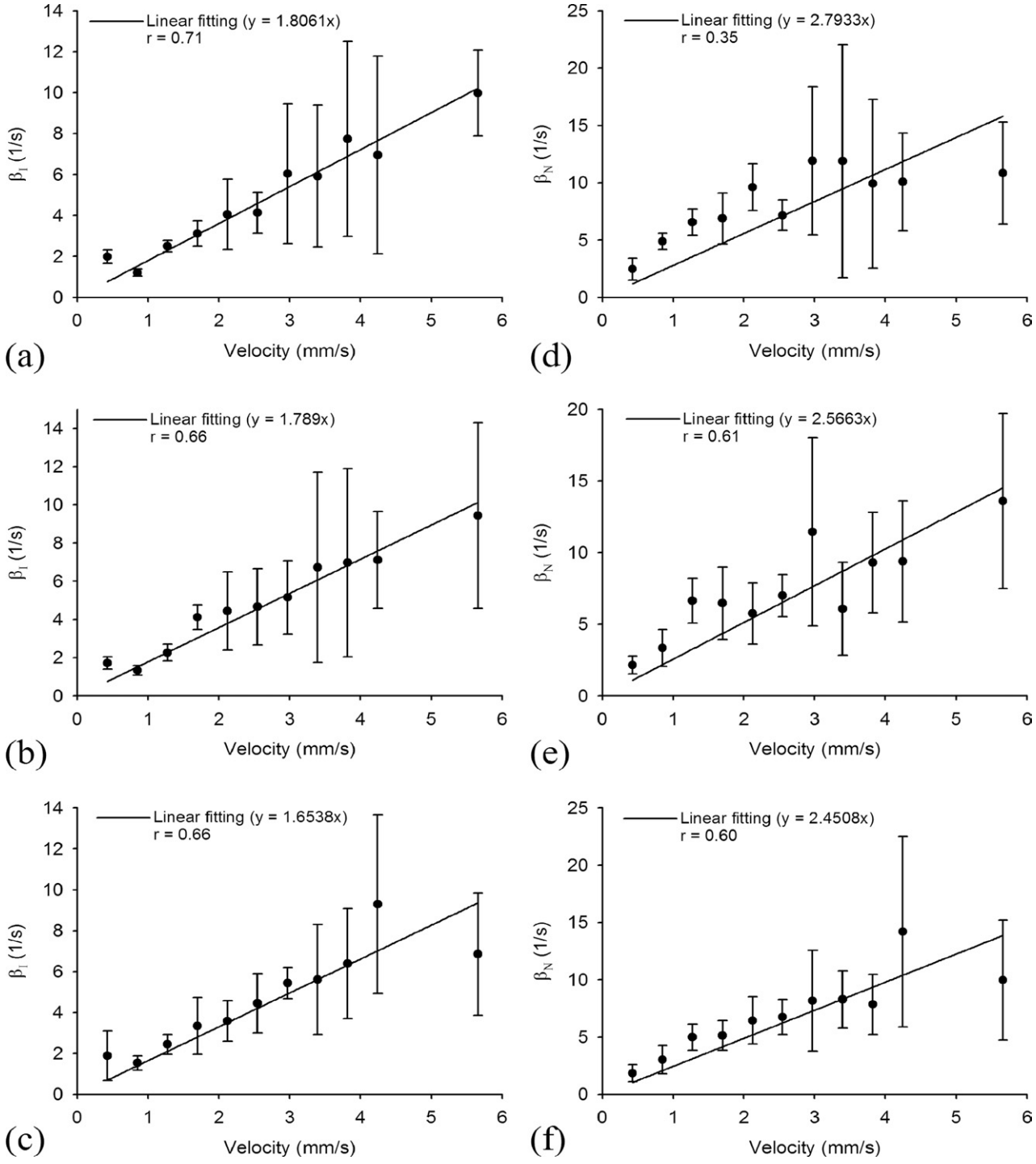

Fig. 5. Rate constants β_I (a) through (c) and β_N (d) through (f) as functions of flow velocity in regions-of-interest (ROIs) at depths of 1.28, 1.92 and 2.56 mm, respectively. Data are mean and SD values.

through f). These experimental results demonstrate that β_N performs similarly to the conventional β_I in quantifying various flow velocities. However, it should be noted that β_N estimation has a larger variance compared to the conventional β_I.

Flow phantom with cotton

Now we use the phantoms with cotton, which is a slightly more accurate model for the *in vivo* situation, to explore the TIC and TNC. The B-mode and Nakagami images of the flow phantom with cotton are shown in

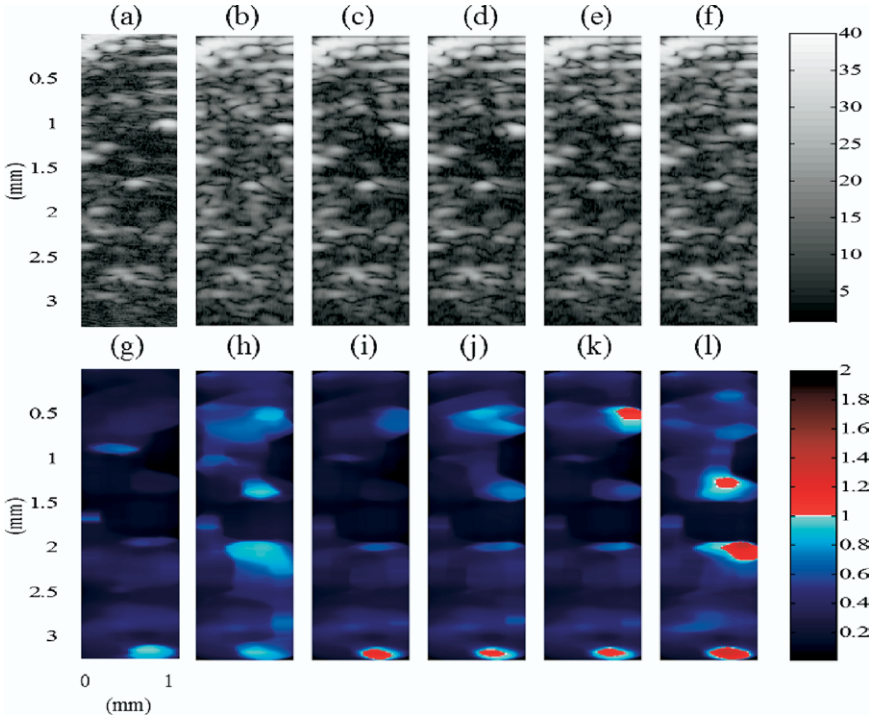

Fig. 6. Typical precontrast (a), postcontrast (b), destruction (c) and replenishment B-mode (d) through (f) and their corresponding Nakagami (g) through (l) images for a flow velocity of 1.27 mm/s (cotton inside the flow phantom).

Fig. 6. The precontrast image is shown in Fig. 6a. Typical B-mode images at acquisition times of 0.7, 2.2, 2.5, 3.0 and 3.6 s are shown in Fig. 6b through f, respectively, also for a flow velocity of 1.27 mm/s. The precontrast image clearly indicates the areas where cotton was present in the flow phantom. The B-mode image of Fig. 6b is slightly brighter where cotton was used to simulate the nonperfused area than where injected microbubbles were present. This image behavior is close to the typical brightness of the B-mode image for the scanning region simultaneously containing the tissue clutter components and the perfusion areas filled with microbubbles. Destruction of the microbubbles by the low-frequency pulse darkens the B-mode image in the perfusion areas, as shown in Fig. 6c and the following replenishment of the microbubbles gradually brightens the B-mode image in the perfusion areas, as indicated by Fig. 6d through f. But the image is always brighter in the cotton-containing nonperfused areas than in the perfusion areas.

The Nakagami images corresponding to the B-mode images in Fig. 6a through f are shown in Fig. 6g through l. The predestruction Nakagami image (Fig. 6h) is dark blue in the cotton-containing nonperfused areas, corresponding to extreme pre-Rayleigh distributions of the backscattered envelope and is light blue to white in the other flow regions containing the microbubbles, corresponding to approximate Rayleigh backscattered statistics. Applying the low-frequency pulses resulted in the shading of the Nakagami image in the perfusion regions varying from light blue and white to dark blue, indicating destruction of the microbubbles in the perfusion areas and the statistical distribution of the ultrasonic backscattered envelope changing from approximate Rayleigh to pre-Rayleigh distributions, as shown in Fig. 6i. Note that the bottom of the flow phantom in the Nakagami image has some red shading, which may be due to the low-frequency pulse not successfully destroying the microbubbles in deep locations when there were several layers of cotton in the flow phantom. With the microbubble replenishment, the perfusion areas of the Nakagami image gradually become light blue and even red, as shown in Fig. 6j through l, indicating that the backscattered statistics varied again from a pre-Rayleigh to an approximately Rayleigh distribution. This reflects an increase in the concentration of replenished microbubbles in the sample volume. Note that the shading remains consistent in the nonperfused areas in the Nakagami image during the replenishment of microbubbles. This is different from the B-mode image, which shows dark-blue shades corresponding to smaller Nakagami parameters than those of the perfusion areas. In other words, the Nakagami image reveals information about flow signals from the microbubbles and simultaneously depresses the information of the nonperfused areas.

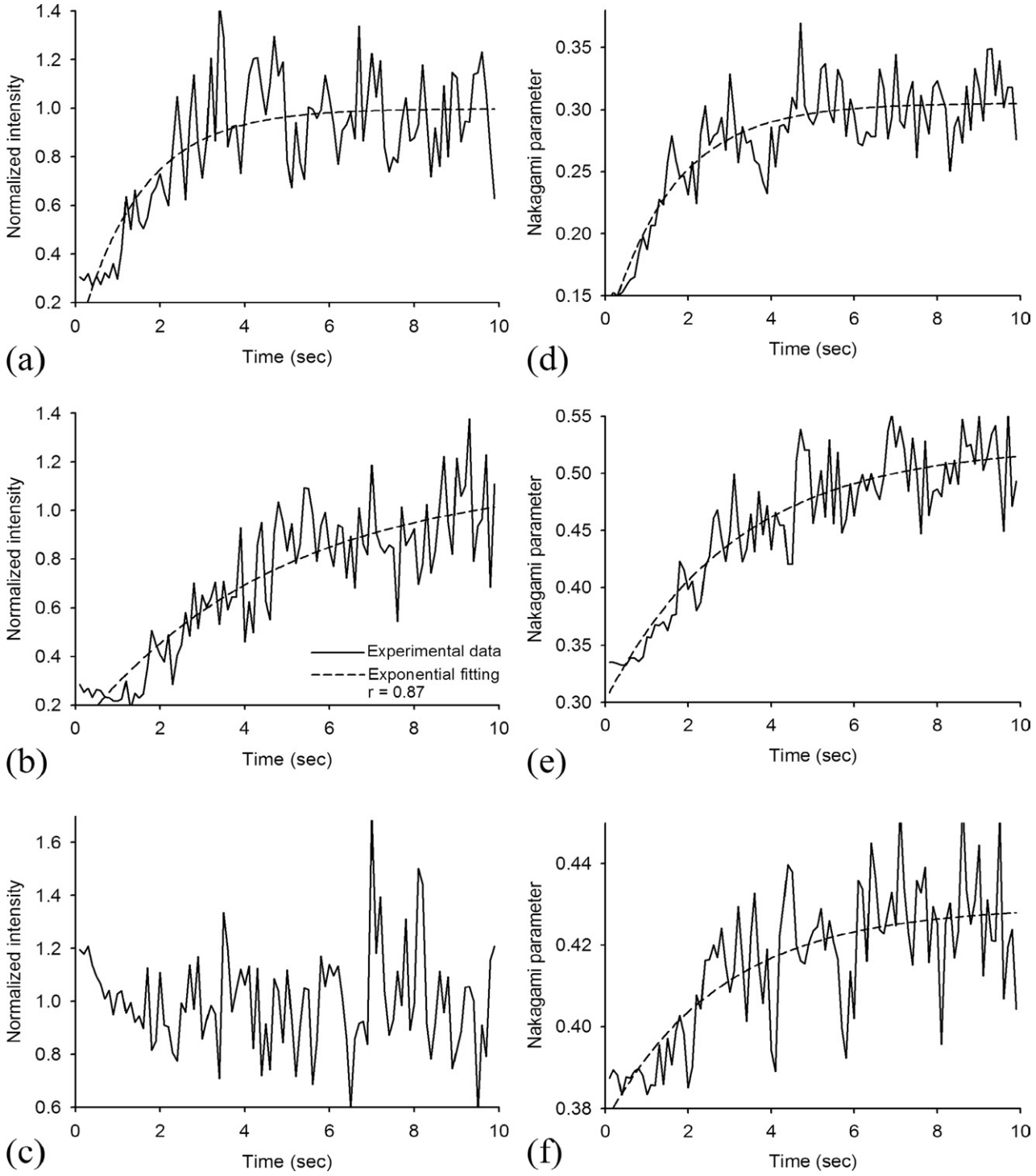

Fig. 7. Time–intensity curves (TICs) (a) through (c) and time–Nakagami-parameter curve (TNCs) (d) through (f) for a flow velocity of 1.27 mm/s in regions-of-interest (ROIs) at depths of 1.28, 1.92 and 2.56 mm (cotton inside the flow phantom).

Typical TICs and TNCs for a flow velocity of 1.27 mm/s in different ROIs obtained from the B-mode and Nakagami images are shown in Fig. 7. Note that for all phantom data, we did not apply wall filtering to remove the components of the signals backscattered from the nonperfused areas, to explore the effects of clutter on the TIC and TNC. For the TICs in ROIs 1 and 2, the normalized backscattering intensity increases exponen-

tially with increasing microbubble replenishment time, as shown in Fig. 7a and b and, thus, these curves can be used to estimate β_I for quantifying the flow velocity. However, the TIC in the deepest ROI (*i.e.,* ROI 3) instead becomes very noisy, making it impossible to fit it with the monoexponential model, as shown in Fig. 7c. Accordingly, the TIC of ROI 3 cannot be used to calculate β_I. The weakness of microbubble signals from deep locations with many clutter components of the flow might explain why ROI 3 did not exhibit the typical exponential shape of the TIC. Considering that the received ultrasonic signals are the summation of the microbubble echoes and the clutter signals, the clutter signals from the nonperfused areas would largely dominate the formation of the TIC during this period and, therefore, information about microbubble replenishment is not obtainable from the TIC. On the other hand, the TNCs in the first two ROIs behave like the TICs, in that they increase exponentially with the replenishment time, as shown in Fig. 7d and e. These TNCs can therefore be used to determine β_N for microvascular flow estimation. It is interesting that the TNC for ROI 3 also increases as a monoexponential with the replenishment time. This may be due to that the TNC only depends on the backscattered statistics rather than the backscattering intensity of microbubble signals, which is weaker and easily hidden in the deepest ROI 3 with many clutter components. Consequently, the TNC is less affected by the clutter signals and using the TNC-based β_N may reduce the influence of clutter signals when estimating the flow velocities at deep locations.

On the other hand, we compared Figs. 4 and 7. It shows that, for both of TIC and TNC, the rise times for the cases without cotton are always faster than those for the cases with cotton. The possible reason lies in that the microbubbles after destruction are difficult to replenish the whole sample volume at a short time under a microcirculation condition that the flow velocity is low and the flowing area has many clutter components. The correction of rise time may be implemented by exploring the relationships between rise time, clutter distribution and density and area size of imaging ROI.

To verify the above-mentioned possible advantage of the TNC technique for measuring the flow at deep locations, we calculated constants β_I and β_N based on the TIC and TNC, respectively, as functions of flow velocity without using wall filtering, as shown in Fig. 8. For the first two ROIs, the average β_I increased from approximately 1/s to 8/s and from 1/s to 4/s as the flow velocity increased from 0.42 to 5.66 mm/s, respectively, as shown in Fig. 8a and b. For the deepest ROI, due to its TIC being very noisy and hence no longer exponential, β_I cannot be determined as a function of flow velocity. On the other hand, the average β_N in ROIs 1 and 2 increased from approximately 1.5/s to 6/s and from 1/s to 3.5/s for the same range of flow velocities, respectively, as shown in Fig. 8c and d. In particular, β_N in ROI 3 increased from about 1/s to 5/s with increasing flow velocity, as shown in Fig. 8e. These results demonstrate that β_I based on the TIC cannot be used for a deep ROI with no wall filtering applied, whereas the TNC-based β_N is more tolerant of the effects of clutter when quantifying different microvascular flow velocities. Furthermore, the comparison between Figs. 5 and 8 shows that the slope of the linear fitting line for β_I and β_N as a function of flow velocity decreases with increasing the image depth, except the case with cotton for β_N in Fig. 8. It implies that β_N can remain sensitive to detect different velocities in deeper locations with clutter effects.

We now propose some explanations for why the Nakagami image is less sensitive to the nonperfused areas and why the TNC for the flow at a deep location still exhibits a monoexponential increase when the ROI contains clutter components. There are some prerequisites for Nakagami imaging successfully suppressing the effects of clutter. First, the tissue clutter size must be much smaller than the sliding window used to construct the Nakagami image (*e.g.,* subresolvable tissue clutter). Second, there should not be too many clutter components in the ROI so that some spacings between tissue clutters can be larger than the sliding window. This can ensure that some microbubble-contributed flow signals be detected by the Nakagami image. Third, the clutter signals should be sufficiently larger or smaller than the microbubble signals. If these three conditions are satisfied, the sliding window will acquire not only tissue echoes but also flow signals when the window moves onto clutter components. Because the clutter signals are larger than the flow signals, the statistics of the backscattered envelopes collected by the window would readily tend to conform to a pre-Rayleigh distribution, making the Nakagami parameter very small. We call this the subresolvable effect of Nakagami imaging, which happens at locations corresponding to clutter components and leads to their depression in the Nakagami image. In this condition, the TNC is accordingly determined by the microbubble flow signals in the ROI. Microbubble replenishment increases the microbubble concentration in the ROI, causing the TNC to increase exponentially with the replenishment time. More importantly, recall that the TNC is determined by the backscattered statistics rather than the backscattered intensity, furnishing the TNC with good performance and making it less affected by weak flow signals from a deep location (with high attenuation).

Whilst the results shown in Figs. 7 and 8 indicate that the tolerance to the effects of clutter is greater for the TNC than for the TIC, this does not necessarily apply to all cases since the clutter components can have diverse

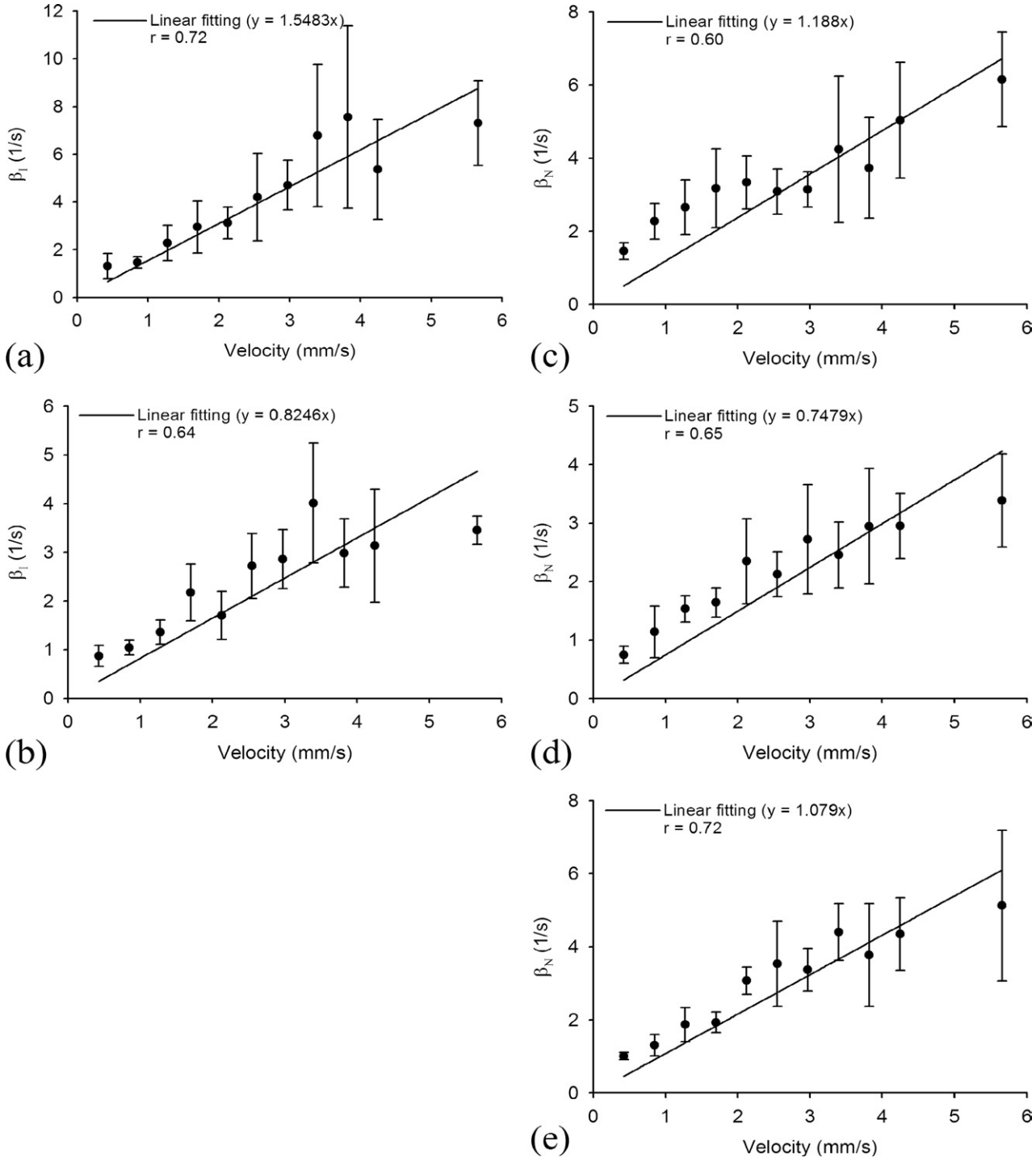

Fig. 8. Rate constants β_I (a) and (b) and β_N (c) through (e) as functions of flow velocity in regions-of-interest (ROIs) at depths of 1.28 and 1.92 mm. Data are mean and SD values.

sizes, shapes and different numbers, arrangements and locations in the ROI. Therefore, to further validate the practical performance of the TNC technique in microcirculation measurements, we performed *in vivo* measurements on rabbit eyes.

Animal experiments

Figure 9 shows precontrast, postcontrast and destruction B-mode images of a rabbit eye. The upper region in the scanning region contained the iris and the lower region contained the ciliary processes. The iris

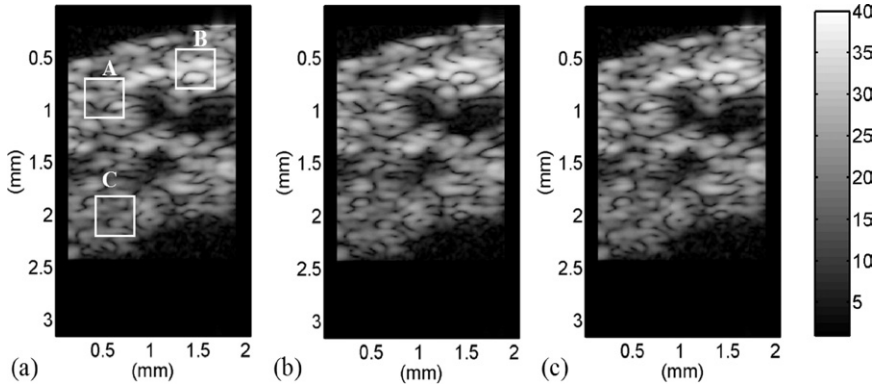

Fig. 9. Typical precontrast (a), postcontrast (b) and destruction (c) B-mode images of a rabbit eye. Regions-of-interest (ROIs) A and B are located in the iris region and ROI C corresponds to the area of marginal capillaries.

contains some arterioles and veins with relatively larger diameters and the ciliary body has marginal capillaries (Ritch et al. 1996). Hence, the average blood flow velocity is higher in the iris region than in the ciliary body, as has been demonstrated previously (Yeh et al. 2004). Note that the recorded signals of a rabbit eye are actually contributed from the injected microbubbles and many tissue clutters with a high echogenicity and, therefore, the three images in Fig. 9 are very similar to each other. Furthermore, no gold standard method for directly measuring blood flow was used in the current study. We examine the *in vivo* results by physiologically theoretical conditions of blood flow in a rabbit eye described above.

To observe the behaviors of the TIC and TNC in regions with different flow velocities, we choose three ROIs in the B-mode image of the rabbit eye: ROIs A and B correspond to upper locations for measuring the iris and ROI C is a deeper location for monitoring the ciliary body. The TICs and TNCs in ROIs A, B and C before wall filtering are shown in Fig. 10. The TICs for all ROIs were very noisy, as shown in Fig. 10a through c. Compared to the phantom results in Fig. 7c, where the TIC is not readily characterizable in deep locations, the TICs in upper locations in a practical tissue microcirculation also are not consistent with a monoexponential function. This may be due to there being too many small vessels of various sizes in the rabbit eye. The clutter contributed by such vessel walls in the ROI may have echo intensities that are larger than those of flow signals contributed by the microbubbles in small vessels. When a wall filter is not used, the formation of the TIC would be dominated by the clutter signals rather than the flow echoes, preventing the rate constant β_I from being calculated to quantify the microvascular flow in the rabbit eye. On the other hand, we found that the TNCs in three ROIs behave similarly to their corresponding TICs in exhibiting very noisy signals, making it impossible to perform exponential fitting to estimate rate constant β_N for distinguishing various flow velocities, as shown in Fig. 10d through f.

In the phantom results in Fig. 7f, the TNC is less influenced by the effects of clutter and still increases exponentially with the microbubble replenishment time even for deep ROIs. However, the results of the animal experiment in Fig.10 appear to disagree with the findings in phantom studies, for which there are several possible reasons. The first is related to the magnitudes of these TNCs. We found that the dynamic ranges for the TNCs ranged between 0.24 and 0.36. These very small Nakagami parameters mean that the statistics of backscattered envelopes in the ROI always remain as pre-Rayleigh distributions during microbubble replenishment. According to the subresolvable effect of Nakagami imaging, it is likely that the ROI is filled with many clutter components so that the generated variation in the backscattered statistics of the flow signals from pre-Rayleigh toward Rayleigh due to microbubble replenishment will become very small. In other words, flow signals embedded in large clutter echoes have no impact on the TNC, which is now fully determined by the clutter echoes for the animal experiments.

The results in Fig. 10 encourage us to further explore the behaviors of the TICs and TNCs of different ROIs after applying the wall filter to remove the effects of clutter from the flow signals. The TICs and TNCs in ROIs A, B and C after wall filtering are shown in Fig. 11. The symbol 'o' denotes $T_{99\%}$, which is the time to 99% replenishment. It is obvious in Fig. 11a and b that using the wall filter results in the TICs in ROIs A and B approximating a monoexponential function that increases with the replenishment of the microbubbles. This demonstrates that wall filtering can remove most of the clutter components so as to yield the typical exponential-based TIC, reflecting the temporal change in ultrasonic backscattering with the microbubble replenishment.

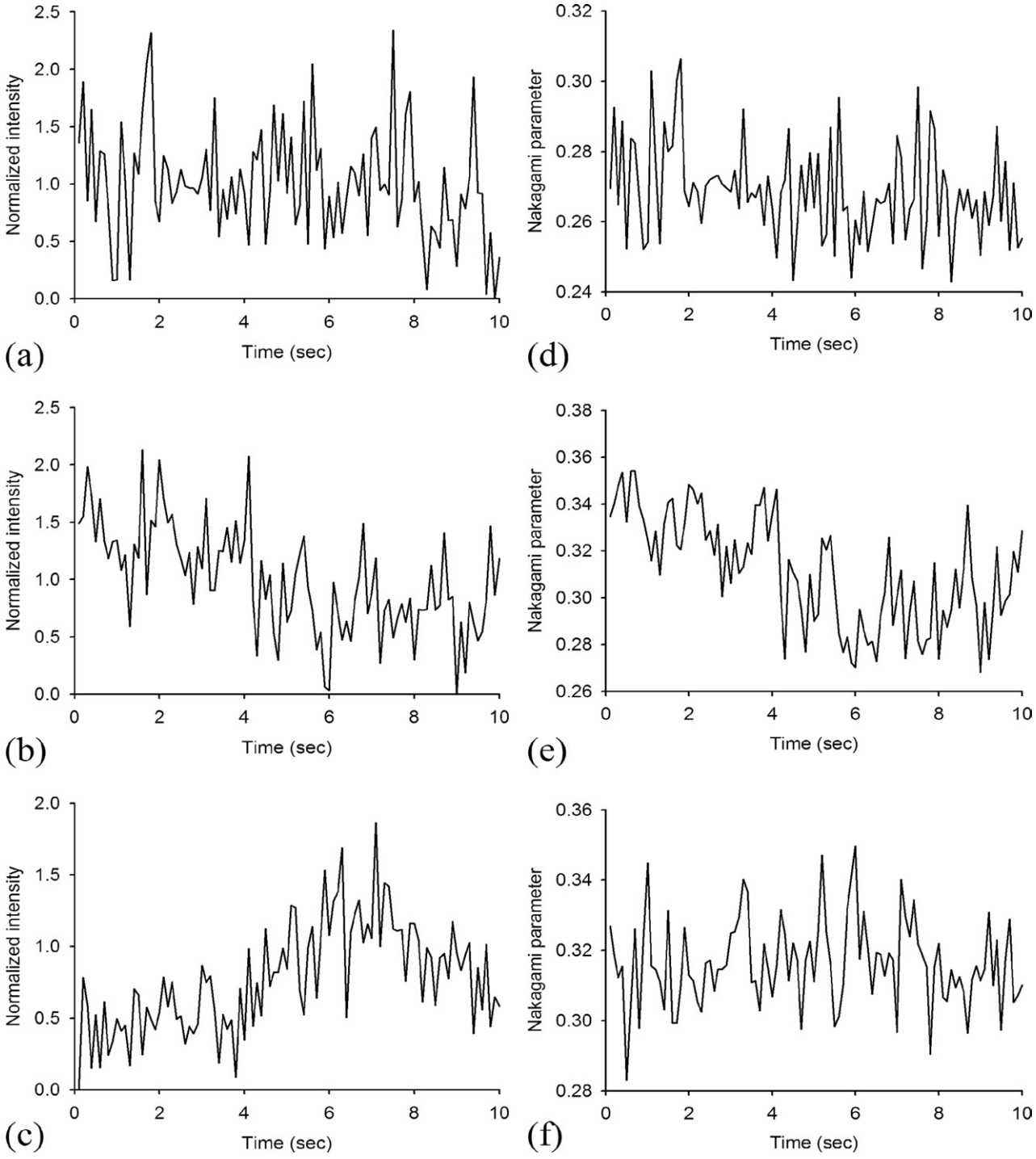

Fig. 10. Time–intensity curves (TICs) (a) through (c) and time–Nakagami-parameter curve (TNCs) (d) through (f) in the rabbit eye before wall filtering in regions-of-interest (ROIs) A, B and C, respectively.

However, for the TIC in ROI C, applying the monoexponential fitting for estimating β_I is difficult due to the curve not exhibiting the typical exponential increase, as shown in Fig. 11c. This is because deep locations are always accompanied by high attenuation, which makes it likely that the flow signals are too weak to form an effective TIC even if the clutter components are fully removed. The TNCs in ROIs A, B and C after wall filtering are shown in Fig. 11d through f, respectively. It was found that the TNCs in ROIs A and B as functions

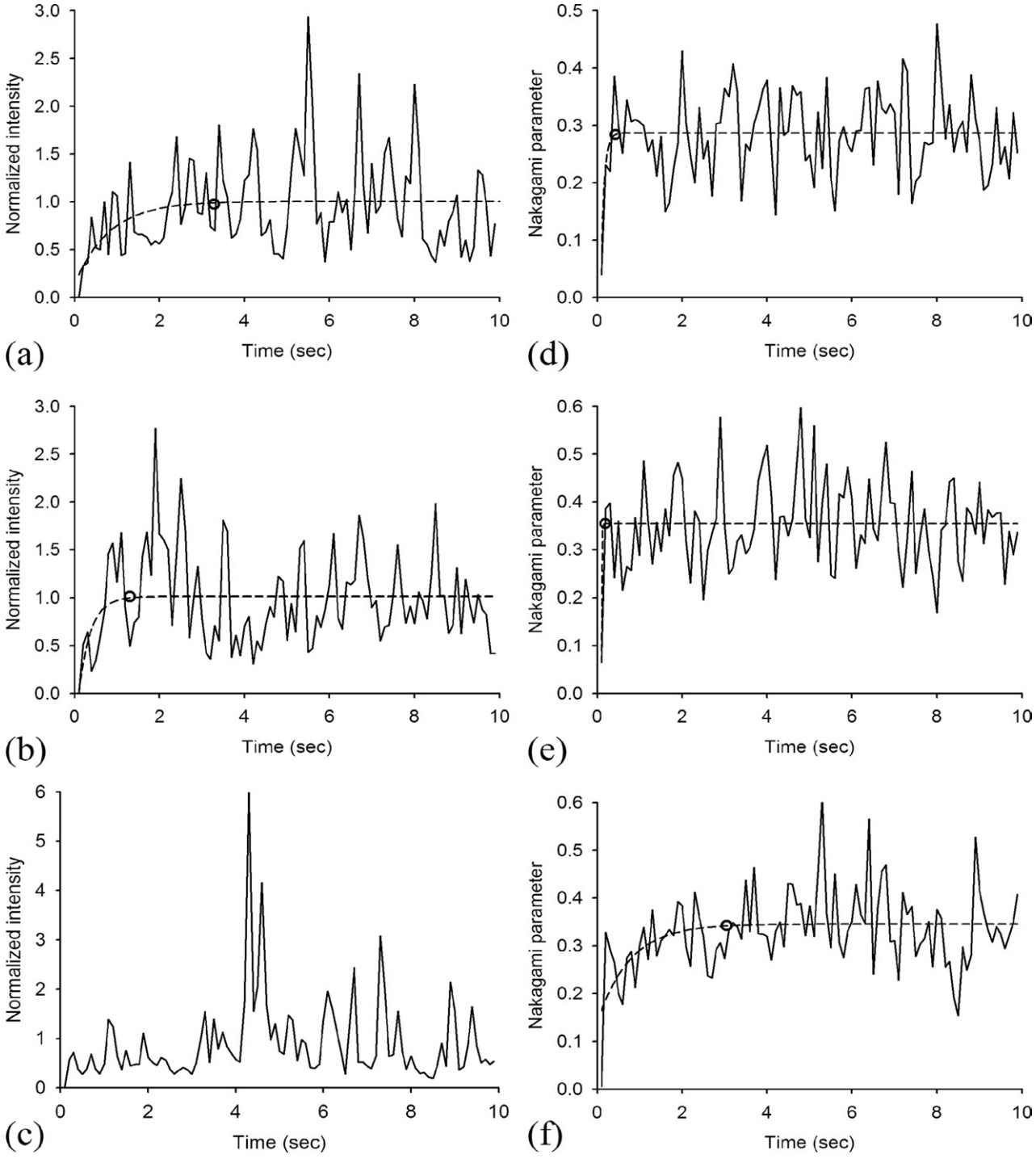

Fig. 11. Time–intensity curves (TICs) (a) through (c) and time–Nakagami-parameter curve (TNCs) (d) through (f) in the rabbit eye after wall filtering in regions-of-interest (ROIs) A, B and C, respectively. The symbol 'o' denotes $T_{99\%}$.

of the replenishment time corresponded well to the monoexponential model, as shown in Fig. 11d and e. Moreover, it is very attractive that the TNC in the deepest ROI (*i.e.,* ROI C) still increases exponentially with the replenishment time, as shown in Fig. 11f. In particular, $T_{99\%}$ is smaller for ROIs A and B than for ROI C, indicating that the flow velocity is higher in the iris region than in the ciliary body. This finding indicates that the TNC conformed to the expected value for microvascular blood flow in real tissues and it further strongly supports our previous declaration that the tolerance to the effects of clutter is greater for the TNC than for the TIC,

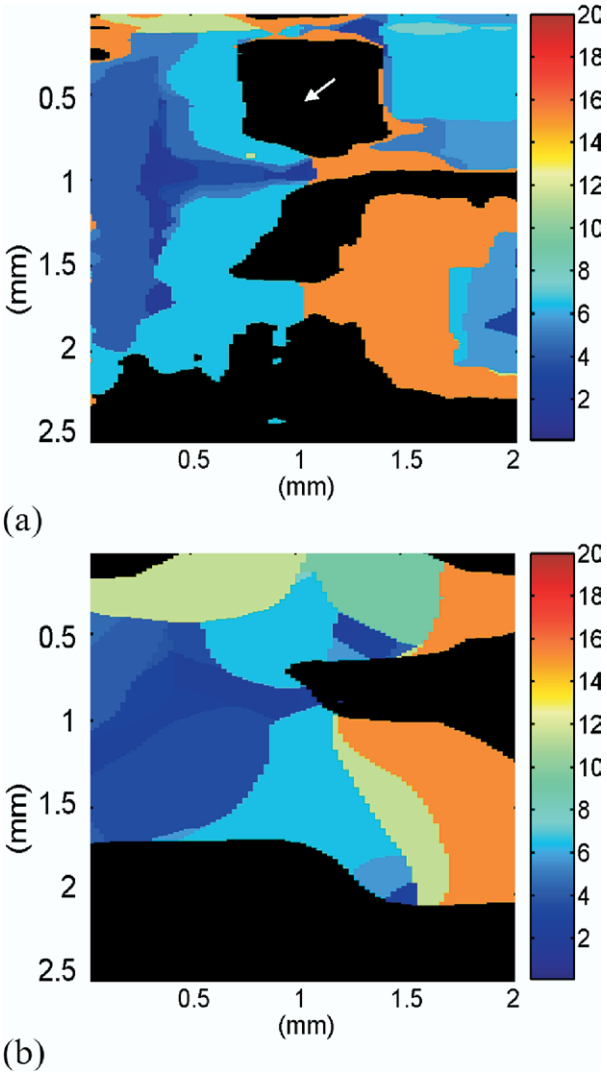

Fig. 12. Flow-velocity parametric images of the rabbit eye after applying wall filtering: β_I (a) and β_N (b). White arrow indicates a perfused region, but the β_I map indicates this as a nonperfused area.

although the results show that a wall filter is still needed when applying the TNC technique in the microcirculation environment.

Figure 12 shows the β_I and β_N parametric images of the scanning region after applying wall filtering, which represent flow-velocity images based on the microbubble destruction and replenishment technique. The black shading in the flow-velocity image indicates nonperfused areas without blood flow (*i.e.,* β_I and β_N equal to 0). As rate constants β_I and β_N increase, the image shading varies from blue to red, representing an increase in the flow velocity. The dynamic ranges for the β_I and β_N parametric images are between 0 and 20. The image profiles in the β_I and β_N maps do not match well with that of the B-scan image of the rabbit eye. This is due to the use of a relatively large sliding window to construct the flow-velocity image ($480 \times 480\ \mu m^2$). A window of this size was used as the minimum region to monitor the flow and calculate the corresponding TNC-based β_N, since this corresponds to the resolution of the Nakagami image (*i.e.,* a square with a side length equal to three times the pulse length). Therefore, compared to using the TIC technique, using the TNC may slightly degrade the resolution and sensitivity of estimating local flows. Note that the β_I image does not reflect the correct information related to the distributions of the blood flow velocities in the rabbit eye. As mentioned above, the flow velocities are higher in the upper region (iris) than in the lower region (ciliary body). However, the β_I image instead indicates that flow velocity is lower in the upper region (blue shading). Moreover, using the β_I map also introduces some errors into estimations of the microvascular flow. For example, the white arrow indicates a perfused region, but the β_I map indicates this as a nonperfused area without blood flow (black shading). Figure 12a shows that the TIC-based method indeed has a limited ability to quantify the microvascular blood flow using high-frequency ultrasound. Compared to the β_I map, the β_N image has a good ability to quantify the flow velocity in the microcirculation. Figure 12b shows that the β_N image correctly indicates that the flow velocity higher in the iris than in the ciliary body. In particular, it was found that using the β_N image has a smaller variability and a more significant meaning ($p < 0.05$) than the β_I image when measuring different regions in the rabbit eye was repeated five times, as shown in Fig. 13 showing that the means and standard deviations of β_I and β_N corresponding to different ROIs.

CONCLUSION

This study employed phantom measurements and *in vivo* experiments on the rabbit eye to explore the more practical performance of using the TNC based on microbubble-contrast-agent-assisted Nakagami imaging to estimate the blood flow velocity in the microcirculation. From the phantom results, we have some findings as follows. First, rate constant β_N obtained from fitting the TNC with a monoexponential model is as useful as the conventional β_I based on the TIC for estimating the flow velocity. Second, based on the subresolvable effect of Nakagami imaging, the use of the TNC is conditionally tolerant of the presence of tissue clutter in the ROI without requiring the application of additional wall filtering.

The *in vivo* animal experiments further produced some important findings and practical considerations. In microcirculation measurements of real tissues, if no wall filter is applied neither the TIC nor the TNC can be used

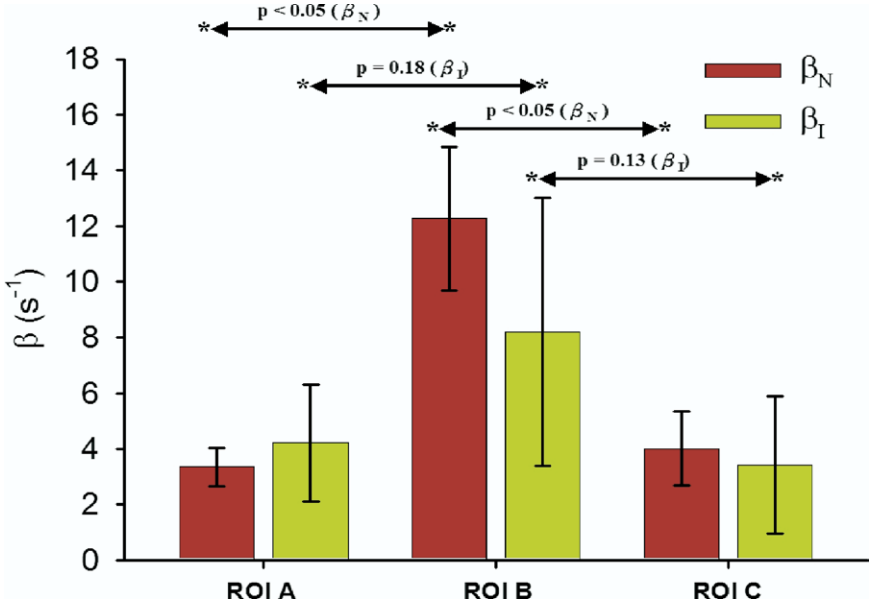

Fig. 13. The means and standard deviations of β_I and β_N corresponding to different region-of-interest (ROIs) for five independent measurements on the rabbit eye.

to estimate β_I and β_N for microvascular flow quantification. This is because the ROI in the tissue microcirculation typically contains many clutter components (*i.e.,* vessel walls of different sizes) and weak microbubble signals, result in the TIC and TNC not exhibiting exponential increases. In this case, it is necessary to apply the wall filter for practical microcirculation measurements in tissues. Under a condition that the wall filter is applied, the β_N image based on the TNC can reflect the physiologically theoretical conditions of blood flow in a rabbit eye but the β_I image based on the conventional TIC cannot. These results suggest that the TNC-based technique can be used as a complementary tool for the conventional TIC method to improve estimation of the microvascular flow.

Acknowledgments—This work was supported by Academia Sinica under Grant No. AS-98-TP-A02 and the National Science Council of the Republic of China (Taiwan) under Grant No. NSC 95-2314-B-007-007-MY3. The authors would like to acknowledge the reviewers for their valuable comments.

REFERENCES

Bjærum S, Torp H, Kristoffersen K. Clutter filter design for ultrasound color flow imaging. IEEE Trans. Ultrason Ferroelectr Freq Control 2002;49:204–216.

Burckhardt CB. Speckle in ultrasound B-mode scans. IEEE Trans Sonics Ultrason 1978;SU-25:1–6.

Chomas JE, Pollard R, Wisner E, Ferrara KW. Subharmonic phase-inversion for tumor perfusion estimation. Proc IEEE Ultrason Symp 2001;2:1713–1716.

Feng N, Zhang J, Wang W. An adaptive clutter rejection method based on AR model in color flow imaging. Ultrasonics 2006;44:e85–e88.

Folberg R, Pe'er J, Gruman LM, Woolson RF, Jeng G, Montague PR, Moninger TO, Yi H, Moore KC. The morphologic characteristics of tumor blood vessels as a marker of tumor progression in primary human uveal melanoma: A matched case-control study. Hum Pathol 1992;23:1298–1305.

Forsberg F, Merton DA, Liu JB, Needleman L, Goldberg BB. Clinical applications of ultrasound contrast agents. Ultrasonics 1998;36: 695–701.

Fung YC. Biomechanics: Circulation. New York: Springer, 1997.

Hampshire JBI, Strohbehn JW, McDaniel MD, Waugh JL, James DH. Probability density of myocardial ultrasonic backscatter. Proceedings of the 14th Annual Northeast Bioengineering Conference. 1988:305–308.

Holfman WC. Statistical methods on radio wave propagation. New York: Pergamon, 1960.

Huang CC, Tsui PH, Wang SH. Detection of coagulating blood under steady flow by statistical analysis of backscattered signals. IEEE Trans Ultrason Ferroelectr Freq Control 2007;54:435–442.

Krix M, Kiessling F, Farhan N, Schmidt K, Hoffend J, Delorme S. A multivessel model describing replenishment kinetics of ultrasound agent for quantification of tissue perfusion. Ultrasound Med Biol 2003;29:1421–1430.

Leong-Poi H, Swales J, Jayaweera AR, Bin JP, Kaul S, Linder JR. Effect of microbubble exposure to ultrasound on quantitation of myocardial perfusion. Echocardiogr 2005;22:503–509.

Lucidarme O, Franchi-Abella S, Correas JM, Bridal SL, Kurtisovski E, Berger G. Blood flow quantification with contrast-enhanced US: "Entrance in the section" phenomenon – phantom and rabbit study. Radiology 2003;228:473–479.

Makitie T, Summanen P, Tarkkanen A, Kivela T. Microvascular density in predicting survival of patients with choroidal and ciliary body melanoma. Invest. Ophthalmol. Vis. Sci. 1999;40:2471–2480.

Metoki R, Moriyasu F, Kamiyama N, Sugimoto K, Iijima H, Xu HX, Aoki T, Miyata Y, Yamamoto K, Kudo K, Shimizu M, Yamada M. Quantification of hepatic parenchymal blood flow by contrast ultrasonography with flash-replenishment imaging. Ultrasound Med Biol 2006;32:1459–1466.

Ritch R, Shields MB, Krupin T. The glaucomas. St. Louis: William C. Brown, 1996.

Schlosser T, Pohl C, Veltmann C, Lohmaier S, Goenechea J, Ehlgen A, Koster J, Bimmel D, Kuntz-Hehner S, Becher H, Tiemann K. Feasibility of the flash-replenishment concept in renal tissue:

Which parameters affect the assessment of the contrast replenishment? Ultrasound Med Biol 2001;27:937–944.

Shankar PM. A general statistical model for ultrasonic backscattering from tissues. IEEE Trans Ultrason Ferroelectr Freq Control 2000; 47:727–736.

Shankar PM, Dumane VA, Reid JM, Genis V, Forsberg F, Piccoli CW, Goldberg BB. Classification of ultrasonic B-mode images of breast masses using Nakagami distribution. IEEE Trans Ultrason Ferroelectr Freq Control 2001;48:569–580.

Silverman RH, Kruse DE, Coleman DJ, Ferrara KW. High-resolution ultrasonic imaging of blood flow in the anterior segment of the eye. Invest Ophthalmol Vis Sci 1999;40:1373–1381.

Tao Q, Wang Y, Fish P, Wang W, Cardoso J. The wall signal removal in Doppler ultrasound systems based on recursive PCA. Ultrasound Med Biol 2004;30:369–379.

Tsui PH, Huang CC, Wang SH, Chiu CY. Quantitative analysis of noise influence on the detection of scatterer concentration by Nakagami parameter. J Med Biol Eng 2005;25:45–51.

Tsui PH, Chang CC. Imaging local scatterer concentrations by the Nakagami statistical model. Ultrasound Med Biol 2007;33:608–619.

Tsui PH, Yeh CK, Chang CC, Chen WS. Performance evaluation of ultrasonic Nakagami image in tissue characterization. Ultrason Imaging 2008;30:78–94.

Wachowiak MP, Smolikova R, Tourassi GD, Elmaghraby AS. General ultrasound speckle models in determining scatterer density. Proc Soc Photo Opt Instrum Eng SPIE 2002;4687:285–295.

Wei K, Jayaweera AR, Firoozan S, Linka A, Skyba DM, Kaul S. Quantification of myocardial blood flow with ultrasound-induced destruction of microbubbles administered as a constant venous infusion. Circulation 1998;97:473–483.

Wei K, Ragosta M, Thorpe J, Coggins M, Moos S, Kaul S. Noninvasive quantification of coronary blood flow reserve in humans using myocardial contrast echocardiography. Circulation 2001;103: 2560–2565.

Weidner N, Semple JP, Welch WR, Folkman J. Tumor angiogenesis and metastasis – correlation in invasive breast carcinoma. New Engl J Med 1991;324:1–7.

Yeh CK, Ferrara KW, Kruse DE. High-resolution functional vascular assessment with ultrasound. IEEE Trans Med Imaging 2004;23: 1263–1275.

Yeh CK, Su SY, Chen WS. Destruction threshold parameters estimation for ultrasonic contrast agents. J Med Biol Eng 2005;25:167–171.

Zimmer Y, Akselrod S, Tepper R. The distribution of the local entropy in ultrasound images. Ultrasound Med Biol 1996;22: 431–439.